

# Processing and Characterization of Extremely Hard and Strong Cu-(0-15 wt pct)Al Alloys



MAHAMMAD ALI SHAIK, BRAHMA RAJU GOLLA,  
and SURESH BABU PITCHUKA

The present work investigates the microstructure development and mechanical properties of mechanically alloyed and hot-pressed copper (Cu)- $X$  wt pct aluminum (Al) ( $X = 0, 3, 5, 10, 15$ ) alloys. The morphology of the ball-milled Cu-Al powders changed from coarse flaky structure to small hard agglomerates with the addition of Al. It was observed that the density of Cu-Al samples varied between  $\sim 95$  and 98 pct of theoretical density ( $\rho_{th}$ ) after hot pressing (Temperature: 500 °C, Pressure: 500 MPa, Time: 30 min). The crystallite size of Cu-Al samples decreased for both the milled powders and hot-pressed samples. The XRD and SEM-EDS analyses of the hot-pressed samples confirmed the presence of  $\alpha$ -Cu solid solution phases for the Cu alloyed with Al up to 5 wt pct. On the other hand, further addition of Al to Cu leads to the formation of both intermetallic compound ( $Cu_9Al_4$ ) and solid solution phase. The nano-indentation tests indicated a significant increase in hardness (2.4 to 7.9 GPa) and elastic modulus (121.1 to 177.4 GPa) of Cu-Al alloys. The Cu-Al alloys were measured with very high compressive strength (813.8 to 1120.2 MPa) and the compressive strain varied in the range of 29.81 to 5.81 pct.

<https://doi.org/10.1007/s11661-019-05545-x>

© The Minerals, Metals & Materials Society and ASM International 2019

## I. INTRODUCTION

COPPER (Cu) alloys have been extensively used for various engineering applications such as naval, rail, aerospace, and automobile industries. In particular, braking and electro-discharge machining (EDM) electrode applications require the development of Cu alloys with high strength, good conductivity and workability, structural stability at high temperatures ( $\sim 200$  °C to 450 °C), good wear, oxidation, and corrosion resistance.<sup>[1,2]</sup> In fact, Cu has been alloyed with alloying elements such as Zn, Sn, Al, W, Fe, Cr, and Zr and these alloys were mainly strengthened by solid solution strengthening or precipitation hardening mechanisms.<sup>[3–8]</sup> Traditionally, these Cu alloys were processed by casting route.<sup>[9]</sup>

One of the major disadvantages of traditional Cu alloys processed by casting route was the coarse grain structure that will lead to poor mechanical properties. Hence, it is required to use alternative processing

techniques in order to control the grain size and improve the mechanical properties of Cu alloys. Severe plastic deformation (SPD) techniques such as high-pressure torsion (HPT),<sup>[8–10]</sup> equal channel angular pressing (ECAP),<sup>[11]</sup> twist extrusion,<sup>[12]</sup> accumulated roll bonding,<sup>[13]</sup> repetitive corrugation and straightening,<sup>[14]</sup> cryo-rolling,<sup>[15]</sup> and friction stir processing (FSP)<sup>[16]</sup> were extensively reported for Cu and its alloys. Powder metallurgy (PM) processes [including Mechanical alloying (MA), spark plasma sintering (SPS)] and additive manufacturing methods [such as selective laser sintering (SLS) and selective laser melting (SLM)] have also been attempted to produce Cu alloys with fine structure.<sup>[4,6,17–20]</sup>

In particular, in view of its nonsparking characteristics, good wear and corrosion resistance, the Cu-Al alloys have potentiality for a range of applications such as welding electrodes, tool material for sheet forming, bearings, rocket nozzle, heat sink, automobile, mining, and naval engineering applications. However, in the literature, studies on Cu-Al alloys have been considerably low and, in particular, systematic investigation of Al effect on the microstructure and mechanical properties of Cu processed *via* PM route. Calvo *et al.*<sup>[21]</sup> studied the effect of pressure and temperature on bonding between Cu and Al. Their work revealed that the bonding between Cu and Al was mainly dominated by diffusion mechanism (between 400 °C and 520 °C and up to 289 hours). The diffusion bonding between

---

MAHAMMAD ALI SHAIK and BRAHMA RAJU GOLLA are with the Metallurgical and Materials Engineering Department, National Institute of Technology, Warangal, 506 004, India. Contact e-mails: gbraju121@gmail.com; gbraju@nitw.ac.in SURESH BABU PITCHUKA is with the International Advanced Research Centre for Powder Metallurgy and New Materials (ARCI) Hyderabad 500005, India.

Manuscript submitted April 24, 2019.

Article published online November 26, 2019

Cu and Al starts reportedly at around 500 °C.<sup>[22]</sup> Chen *et al.*<sup>[23]</sup> proposed the diffusion mechanism in Cu-Al alloy system and the high diffusion rate of Al results in the formation of the saturated solid solution at the interface of Cu and Al. The structure of interface consists of different intermediate phases such as CuAl<sub>2</sub>, Cu<sub>9</sub>Al<sub>4</sub>, CuAl, Cu<sub>4</sub>Al<sub>3</sub>, and Cu<sub>3</sub>Al<sub>2</sub>. In another work, Wu *et al.*<sup>[24]</sup> refined the microstructure by reducing the diffusion coefficient with the application of high-pressure (5 GPa) heat treatment at 750 °C for 15 minutes. Wang *et al.*<sup>[25]</sup> stated that high-pressure heat treatment favors the formation of a fine structure as it reduces the solid phase transformation temperature and activation energy.

In this work, we made an attempt to process the mechanically alloyed Cu-Al alloys through the hot pressing route. The Cu alloys were consolidated relatively at a low sintering temperature of 500 °C with the application of high hot press pressure of 500 MPa in a vacuum environment. The high-pressure processes are reportedly advantageous as they facilitate high nucleation rate, reduce atomic diffusion coefficient, restrain grain growth, and result in refinement of grain structure.<sup>[24,25]</sup> The major objectives of the present investigation are to (i) process the Cu-Al alloys by mechanical alloying and densifying them through hot pressing route with high-pressure application; (ii) study its effect on microstructure of Cu-Al alloys; (iii) improve mechanical properties (hardness and strength) of the Cu alloys, (iv) structure-property correlation of Cu-Al alloys and (v) compare the measured mechanical properties of the developed Cu-Al alloys with the existing literature.

## II. EXPERIMENTAL DETAILS

### A. Mechanical Alloying of Cu-Al Powders

Commercial copper (Padmasree enterprises, Hyderabad, India) and aluminum powders (SRL™, India) with a mean particle size less than 45 μm and purity greater than 99 pct were (as per the supplier's data) used as starting materials in the present study. From SEM analysis, it was observed that the Cu powders are spherical in shape with a mean particle size of ~ 9.98 μm and Al powders are characterized with irregular particle shape and with the size of ~ 6.47 μm (Figure 1).

Appropriate amounts of Al powders were added to Cu and the compositions were mechanically alloyed with a planetary ball mill (Model: PM400, Retsch GmbH) to prepare Cu-*X* wt pct Al (*X* = 0, 3, 5, 10, and 15) nominal compositions; they were referred as Cu, Cu-3Al, Cu-5Al, Cu-10Al, and Cu-15Al. From the available literature of Cu alloys and composites, it was observed that the milling of Cu-based materials carried out at a milling speed in the range between 120 and 600 rpm, milling time between 1 and 50 hours, and ball-to-powder weight ratio (BPR) ranging from 1.5:1 to 10:1.<sup>[26–29]</sup> Based on the literature and our preliminary experiments, in the present work, milling parameters were selected to reduce the particle size and to ensure uniform mixing and dispersion of Al in Cu. The

elemental powders were milled in stainless steel vials for 10 hours duration at 260 rpm (Ball-to-Powder ratio is 10:1), using toluene as dispersing medium. The milling was programmed with a dwell time for 10 minutes and run time for 10 minutes in cyclic to avoid overheating of vials. The ball-milled powders were dried using rotary vacuum evaporator (RV10, IKA, Germany) at 98 °C for 30 minutes.

### B. Processing of the Bulk Cu-Al Alloys

The ball-milled Cu-Al alloys were consolidated using a hot press (Model: CMM, VB Ceramic Consultants, India) at a sintering temperature of 500 °C under hydraulic ram pressure of 500 MPa for 30 minutes in vacuum ( $1.3 \times 10^{-2}$  mbar) environment. The heating rate during the heating cycle of hot pressing was programmed at 10 °C/min and after furnace cooling, the sintered samples were ejected from the H13 steel die at room temperature. The samples were prepared with the dimensions of 15 mm in diameter and 5 mm height. The density measurements of Cu-Al samples were carried out by using a precision weighing balance attached to the density measurement setup (Model: BSA224S-CW, Sartorius). The bulk density of compacts was measured by the Archimedes technique according to ASTM B962-08. To compare the densification response of various compositions, the bulk densities were normalized with respect to theoretical density.

### C. Microstructural Characterization

The microstructure of powders and hot-pressed samples was carried out by means of the scanning electron microscope (SEM: TESCAN VEGA 3 LMU). The compositional analysis of Cu-Al alloys was carried out by energy dispersive spectroscopy (EDS: Oxford Instruments). Metallographic sample preparation was done to reveal the microstructure of hot-pressed samples. The polishing of samples was carried out using grinding, disc polishing with silicon carbide papers up to 2000 grade and they were further polished to mirror finish by using alumina liquid suspension. The surface of these samples was etched with HNO<sub>3</sub> (50 pct) and distilled water (50 pct) solution for a few seconds. The microstructural characterization of etched and fracture surface of Cu-Al samples was inspected with SEM-EDS. The phase analysis of starting, milled powders, and the sintered compacts was carried out by X-ray diffraction (XPert-Pro, Pan Analytical), using CuK<sub>α</sub> radiation ( $\lambda = 1.5405 \text{ \AA}$ ), which was operated at 45 kV and 30 mA. The volume fraction of individual phases in the hot-pressed samples was estimated by the Rietveld analysis of XRD patterns. The XRD data were collected at a scanning rate of 0.0166 °/s and the patterns analyzed by X'pert High Score software with Inorganic Crystal Structure Database (ICSD). For dislocation density measurements, the curve was fitted after stripping the K $\alpha$ 2 component from the raw data using X'Pert High score software. The full-width half maximum (FWHM) values and diffraction angles of major peaks

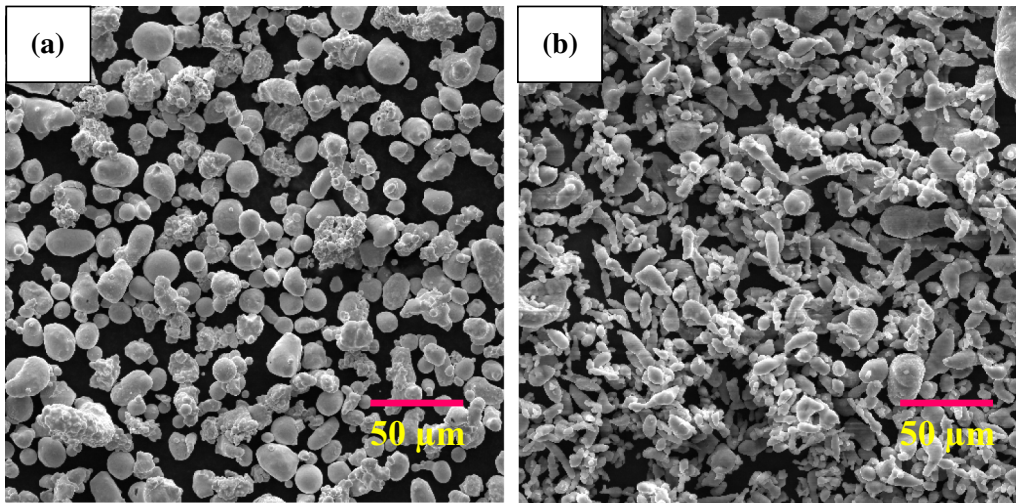


Fig. 1—SEM images of as received (a) copper (mean size of  $\sim 9.98 \mu\text{m}$ ) and (b) aluminum powders (mean size of  $\sim 6.47 \mu\text{m}$ ).

from the X-ray diffraction patterns were considered for Williamson–Hall analysis.

#### D. Mechanical Properties Measurement

The hardness of polished samples was measured using Vickers Micro-hardness tester (Shimadzu, HMV, Japan) at 100 g load for 30 seconds according to ASTM E384-11e1. A minimum of five indentations was made to evaluate the hardness. Further nano-indentation test was used to understand load-displacement behavior, elastic and plastic properties of alloys. Before the nano-indentation test, the samples were finely polished using colloidal silica suspension for 2 hours to get the good surface finish and the nano-indentation test (Model: Nano Test Vantage, Micro Materials, UK) was carried out using Berkovich indenter. The test was performed at a constant load of 20 mN with a loading and unloading rate of 2.0 mN/s. The area (an array of  $10 \times 10$  matrix with  $40 \mu\text{m}$  spacing) was selected on the sample surface such that 100 indentations could be made to get good representative data. The compression test of Cu-Al alloys was conducted on the Universal Testing Machine (UTM) (Instron, Model No: 5982) at a strain rate of 0.02 mm/min. In order to minimize the friction during the compression test, grease was applied on the top and bottom specimen–platen interfaces. The cylindrical samples having the dimensions of 10 mm diameter ( $d$ ) and 15 mm length ( $l$ ) with  $l/d$  ratio of 1.5 were prepared for the compression test. A minimum of two measurements was taken for reporting the compression results.

### III. RESULTS AND DISCUSSION

#### A. Microstructural Characterization

The copper powders are of spherical shape and the morphology of aluminum powder particles is observed to be semi-spherical and in the elongated form

(Figure 1). During the ball milling, the elemental Cu powders deformed into flaky shape due to its cold welding (see Figure 2(a)). The mean particle size of Cu-Al compositions after 10 hours mechanical milling was estimated based on the SEM images. The particle size of Cu reduced from  $84.3$  to  $9.2 \mu\text{m}$  with the addition of Al (pure copper:  $84.3 \pm 8 \mu\text{m}$ , Cu-3Al:  $75.1 \pm 9 \mu\text{m}$ , Cu-5Al:  $47.4 \pm 5 \mu\text{m}$ , Cu-10Al:  $17.6 \pm 1 \mu\text{m}$ , and Cu-15Al:  $9.2 \pm 0.9 \mu\text{m}$ ). The particle–particle cold welding in pure Cu might be leading to the formation of large flakes. However, the flaky size of Cu reduced considerably and hard agglomerates formed with the addition of Al as it can be clearly seen in Figure 2(a) through (d). With the increasing addition of Al to Cu, the size of agglomerated particles reduced due to continuous fracture and cold welding.

The presence of fine agglomerates in Cu-Al compositions indicates relatively easy fragmentation of aggregates than in pure Cu. As the Al content increased, the size of flakes and agglomerates got reduced due to its continuous impact, cold welding, fracture, re-welding, and solid solution formation during ball milling. The particle welding in Cu-Al during milling might be hindered due to the formation of Cu-Al solid solution (see Figure 3) and fragmentation of agglomerates.

The corresponding X-ray diffraction patterns of ball-milled Cu-Al powders are presented in Figure 3. During the ball milling process, the copper-rich solid solution  $\alpha$ -Cu ( $\text{Cu}_{0.92}\text{Al}_{0.08}$ ) with a small amount of aluminum was noticed in all alloy powders. The peak intensity of Cu for the alloys was observed to decrease as the Al content increased and peak shift (which can be attributed to the formation of the solid solution), internal stress, and grain refinement by cold deformation. The X-ray diffraction patterns of hot-pressed samples are presented in Figure 4.

The XRD patterns of Cu- $X$  wt pct Al ( $X = 0, 3, 5, 10,$  and  $15$ ) sintered samples revealed the presence of  $\alpha$ -Cu ( $\text{Cu}_{0.92}\text{Al}_{0.08}$ ),  $\alpha$  ( $\text{Cu}_{0.78}\text{Al}_{0.22}$ ), and  $\gamma_2$  ( $\text{Cu}_9\text{Al}_4$ ) phases. According to the Cu-Al equilibrium phase diagram,  $\alpha$ -Cu solid solution formation is expected up



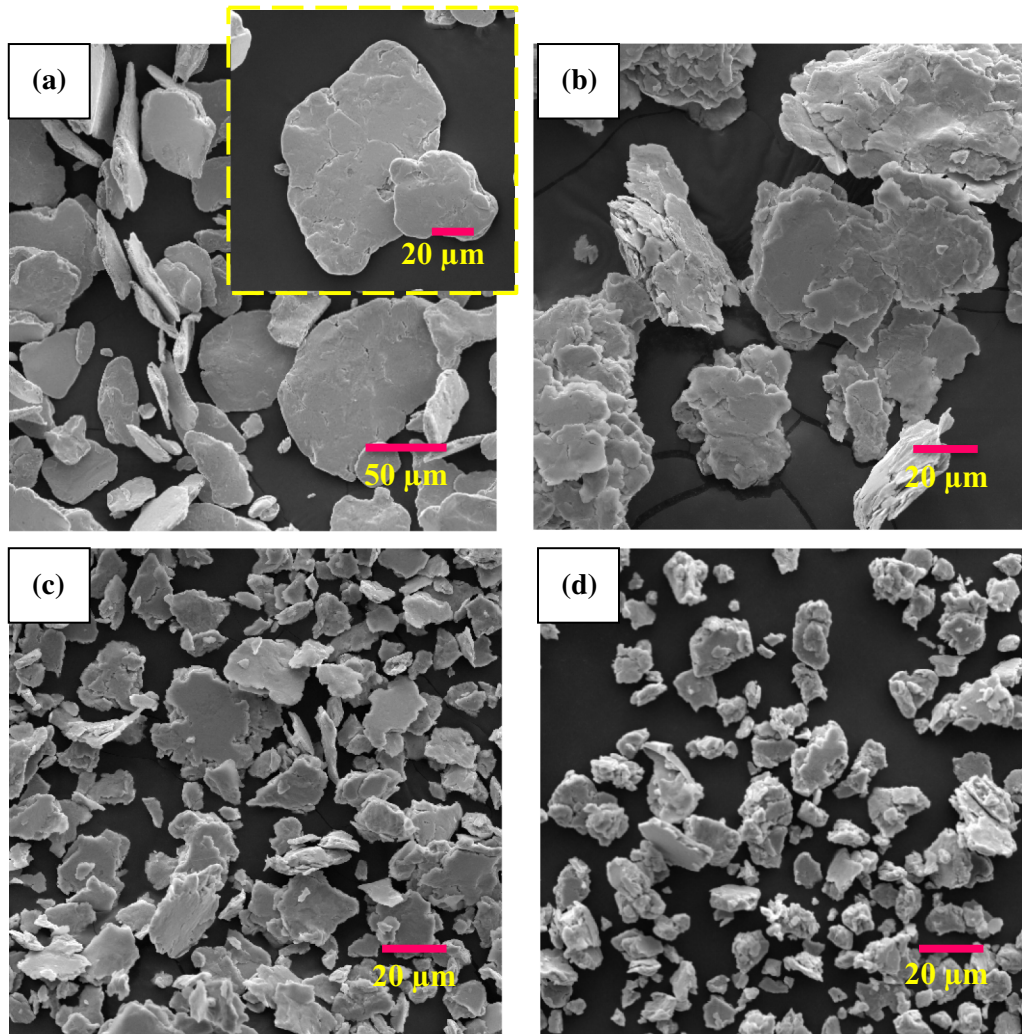


Fig. 2—SEM images milled powders after 10-h ball milling at 260 rpm. (a) Cu, (b) Cu-5Al, (c) Cu-10Al, and (d) Cu-15Al. The transition of flake-like shape to small aggregates has been seen as Al content increased.

to 9.4 wt pct Al addition and  $\alpha$  solid solution, and  $\gamma_2$  intermetallic phases from 9.4 to 15.6 wt pct Al addition to Cu.<sup>[22,30]</sup> The phases that were formed in the hot-pressed Cu-Al alloys are similar to the phases of the Cu-Al phase diagram. The quantification of XRD phases was carried out through Rietveld analysis using X'Pert High Score software.

The results obtained from the XRD patterns of hot-pressed are given in Table I. In case of Cu-3Al and Cu-5Al alloys, the  $\alpha$ -Cu solid solution was the only phase identified from the XRD.

On the other hand, the formation of major  $\alpha$  phase (86.6 wt pct) and minor  $\gamma_2$  phase (13.4 wt pct) for Cu-10Al and the presence of  $\gamma_2$  major phase (75.3 wt pct) along with  $\alpha$  (24.7 wt pct) were identified for Cu-15Al. To further confirm the presence of these phases in the Cu-Al alloys, Bragg's law was used to estimate the lattice parameter ( $a$ ) of each phase from the XRD analysis (using Eqs. [1] to [2]), which was compared with the standard lattice parameter (JCPDS), where wavelength ( $\lambda$ ), diffraction angle ( $2\theta$ ), interplanar spacing ( $d$ ), and Miller indices ( $hkl$ ) were related to

Cu-Al alloy diffraction peaks. The lattice parameters measured from the XRD patterns of Cu-Al alloys and their corresponding JCPDS values are specified in Table II.

$$d = \frac{n\lambda}{2 \sin \theta} \quad [1]$$

$$a = \frac{d}{\sqrt{(h^2 + k^2 + l^2)}} \quad [2]$$

The strong XRD patterns were selected to calculate the lattice parameter ( $a$ ). The lattice parameter of  $\alpha$ -Cu phase at its major peak was calculated to be 0.3632 to 0.3642 nm, for  $\alpha$  phase: 0.3605 to 0.3648 nm, and for  $\gamma_2$  phase: 0.868 to 0.8715 nm. These lattice parameter values are in good agreement with the JCPDS values and thus match the presence of  $\alpha$ -Cu,  $\alpha$ , and  $\gamma_2$  phases in the Cu-Al sintered alloys.

Figure 5 presents the representative microstructure of etched Cu-3Al and Cu-5Al alloys. The SE and BSE

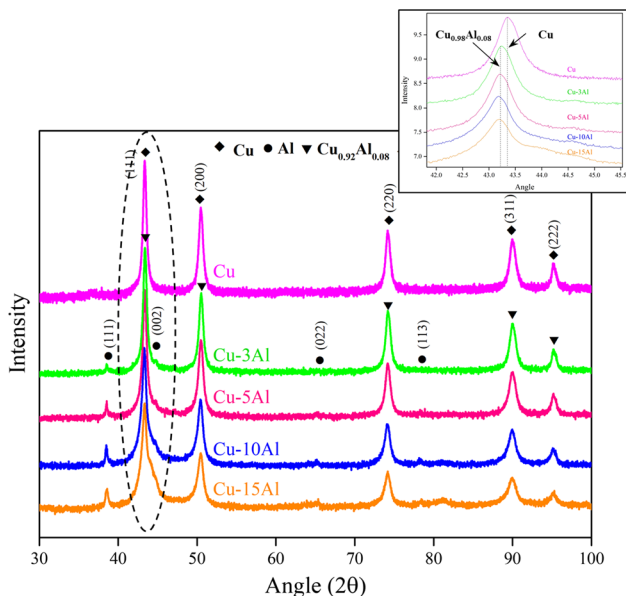


Fig. 3—Comparison of X-ray diffraction patterns of Cu- $X$  wt pct Al milled powders (260 rpm, 10 h), where the nominal composition ( $X$ ) of Al alloying element is ranging from 0 to 15 wt pct. The inset diagram shows a peak shift of Cu with the addition of Al and indicates the solid solution formation.

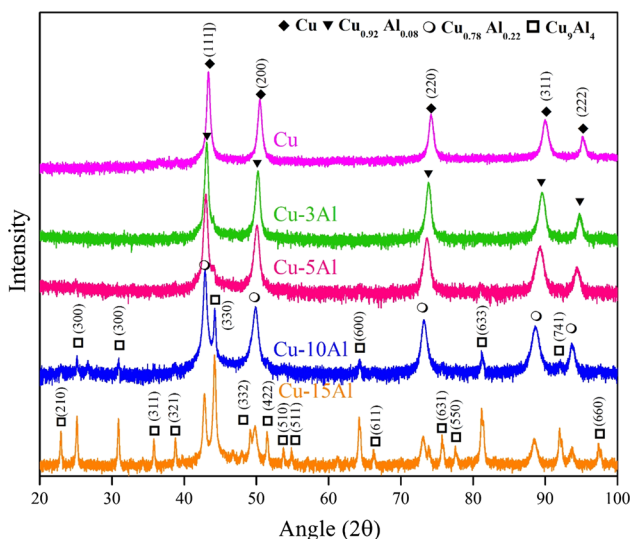


Fig. 4—Comparison of X-ray diffraction patterns of hot-pressed Cu- $X$  wt pct Al alloys (hot press conditions: 500 °C, 500 MPa, 30 min), where the nominal composition ( $X$ ) of Al alloying element is ranging from 0 to 15 wt pct.

**Table I. Densification and Microstructural Phases of Hot-Pressed Cu-Al Alloys**

Sample Reference	Theoretical Density (g/cc)	Bulk Density (g/cc)	Relative Density (Pct)	XRD Phases	Wt Pct of Phase Based on Rietveld Analysis of XRD Patterns
Cu	8.96	8.84	98.66	Cu	100
Cu-3Al	8.38	8.07	96.30	Cu <sub>0.92</sub> Al <sub>0.08</sub>	100
Cu-5Al	8.38	7.97	95.16	Cu <sub>0.92</sub> Al <sub>0.08</sub>	100
Cu-10Al	7.37	7.01	95.10	Cu <sub>0.78</sub> Al <sub>0.22</sub>	86.60
				Cu <sub>9</sub> Al <sub>4</sub>	13.30
Cu-15Al	6.98	6.61	94.60	Cu <sub>0.78</sub> Al <sub>0.22</sub>	24.70
				Cu <sub>9</sub> Al <sub>4</sub>	75.30

images of both the alloys reveal the presence of a single constituent phase ( $\alpha$ -Cu solid solution) in its microstructure. It can be observed that the grain size of Cu-3Al is relatively coarser than Cu-5Al. The corresponding SEM-EDS confirms the presence of Cu and Al elements, which validates the presence of  $\alpha$ -Cu (Cu<sub>0.92</sub>Al<sub>0.08</sub>) solid solution phase.

The BSE-SEM images show the presence of bright gray (unetched regions: 1) and dark gray contrasting phases (etched regions: 2) in a Cu-15Al alloy as shown in Figure 6. The EDS compositional analysis of the two contrasting phases reveals that these phases are measured with different amounts of Al content. The quantification of elements from different phases in Cu-Al alloys is listed in Figure 6 (inset). From SEM-EDS results, Cu-15Al alloy consists of bright and dark gray regions, which are identified as  $\alpha$  (Cu<sub>0.78</sub>Al<sub>0.22</sub>) and  $\gamma_2$  (Cu<sub>9</sub>Al<sub>4</sub>) phases, respectively. From the Cu-Al equilibrium phase diagram, the solid solution  $\alpha$  phase completely dissolves up to 9.4 wt pct of Al.<sup>[31,32]</sup> According to Eq. [3], the  $\beta$  phase transforms into the  $\alpha$  and  $\gamma_2$  phases at the eutectoid reaction (Eq. [3]). At a temperature of 500 °C, a maximum amount of aluminum (up to 15.6 pct) dissolves in copper and forms  $\gamma_2$  phase.<sup>[33]</sup> Therefore, the excess amount of Al leads to formation  $\gamma_2$  phase in Cu-10Al and Cu-15Al alloys.

In the present work,  $\gamma_2$  intermetallic phase formation is evident for both Cu-10Al and Cu-15Al alloys. Similar observations were reported for die-casted Cu-11.8 wt pct Al alloy that forms  $\gamma_2$  phase by eutectoid decomposition of  $\beta$  phase at a temperature of 565 °C.<sup>[34]</sup>

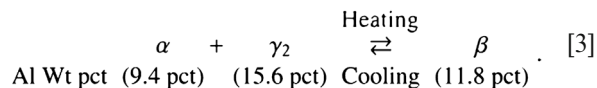


Figure 7 shows the SEM images of fracture surfaces of Cu-Al hot-pressed samples. Both pure copper and alloys consist of the mixed mode of fracture (the samples were fractured manually with a hammer to observe the microstructure). A careful look at Figure 7 indicates that the pct of intergranular fracture increased with the addition of Al to Cu (Figure 7). It also should be clear that the fineness of grains increased with the addition of Al to Cu.

### B. Densification of Cu-Al Alloys

Since aluminum is a light metal with considerably low density (2.73 g/cc) when compared to copper (8.96 g/cc), it is expected that the addition of aluminum significantly



**Table II. Crystallographic Information of Hot-Pressed Cu-Al Alloys Obtained from the XRD Patterns**

Sample Reference	XRD Phases	Crystal Structure	Interplanar Space, $d$ (nm)	Miller Indices (hkl)	Calculated Lattice Parameter, $a$ (nm)	Lattice Parameter from JCPDS, $a$ (nm)
Cu	Cu	FCC	0.2097	111	0.3632	0.3616
Cu-3Al	$\text{Cu}_{0.92}\text{Al}_{0.08}$	FCC	0.2098	111	0.3632	0.3634
Cu-5Al	$\text{Cu}_{0.92}\text{Al}_{0.08}$	FCC	0.2098	111	0.3642	0.3634
Cu-10Al	$\text{Cu}_{0.78}\text{Al}_{0.22}$	FCC	0.2119	111	0.3648	0.367
	$\text{Cu}_9\text{Al}_4$	complex cubic	0.2051	330	0.8680	0.8702
Cu-15Al	$\text{Cu}_{0.78}\text{Al}_{0.22}$	FCC	0.2119	111	0.3605	0.367
	$\text{Cu}_9\text{Al}_4$	complex cubic	0.2051	330	0.8685	0.8702

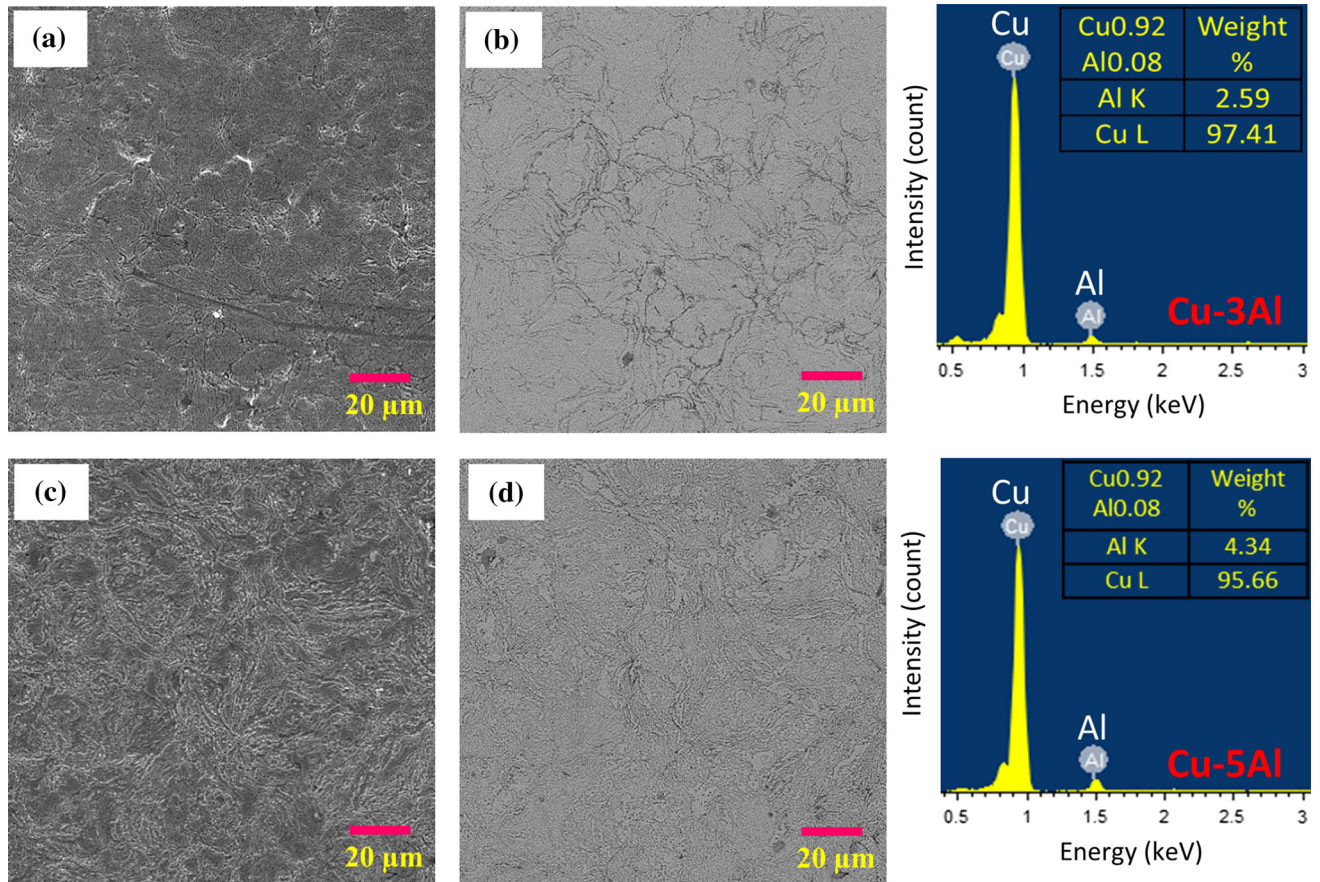


Fig. 5—SEM images of Cu-Al hot-pressed samples (at 500 °C, 500 MPa, 30 min under vacuum). (a) and (b) The microstructure (SE and BSE images) of Cu-3Al alloy and (c) and (d) the SE and BSE images of Cu-5Al alloy. The corresponding EDS of alloys is shown along with elemental compositions.

lowers the density of Cu alloys. The density and corresponding hardness of the hot-pressed Cu-Al alloys as a function of Al content are shown in Figure 8.

To calculate theoretical densities of Cu-Al alloys, the densities of  $\text{Cu}_{0.92}\text{Al}_{0.08}$ ,<sup>[35]</sup>  $\text{Cu}_{0.78}\text{Al}_{0.22}$ ,<sup>[36]</sup> and  $\text{Cu}_9\text{Al}_4$ <sup>[37]</sup> phases were taken as 8.39 g/cc, 7.46 g/cc, and 6.84 g/cc, respectively. The theoretical density was calculated using the rule of the mixture and the relative amount of phases in the alloy (that were estimated by the Rietveld analysis of XRD patterns) (Table I). The theoretical density ( $\rho_{\text{th}}$ ) of Cu-Al alloys was observed to

decrease from 8.96 to 6.98 g/cc with the addition of Al (up to 15 wt pct) and the measured experimental/bulk density of samples varied between 8.84 and 6.61 g/cc. From Table I, it is evident that pure Cu could be densified to 98.66 pct  $\rho_{\text{th}}$  and the relative density of Cu-Al alloys observed to vary between ~ 95 and 96 pct  $\rho_{\text{th}}$  depending on the Al content. The decrease in density of Cu with Al addition can be attributed to hard agglomerates (ball-milled powders) and intermetallic phase formation during sintering, which might have hindered the densification. Among all Cu alloys,

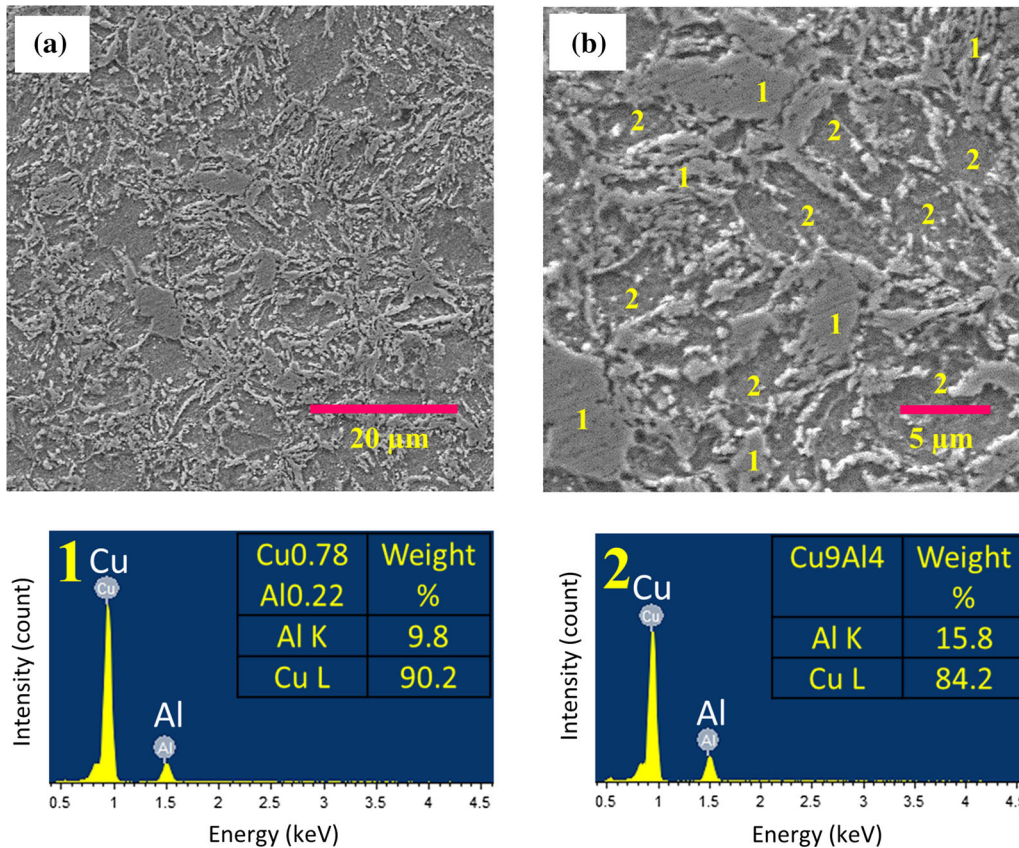


Fig. 6—SEM (BSE) images of Cu-15Al hot-pressed samples (at 500 °C, 500 MPa, 30 min under vacuum) having different phases. (a) Low-magnification and (b) high-magnification images. The corresponding EDS analysis of phases is also shown. (1, Unetched regions: Cu<sub>0.78</sub>Al<sub>0.22</sub>; 2, Etched regions: Cu<sub>9</sub>Al<sub>4</sub>).

Cu-15Al composed of finer grain structure with a relatively low density of 94.6 pct  $\rho_{th}$ . The densification of Cu samples can be attributed to mechanical milling, solid-state sintering, and large plastic deformations due to the milling and application of high pressure during hot pressing.

It has to be noted here that Rajkovic *et al.*<sup>[38]</sup> could achieve a maximum density of 85.1 pct  $\rho_{th}$  for hot-pressed Cu-3.5Al even after using high sintering temperature of 800 °C and the pressure of 35 MPa for 1 hour. He *et al.*<sup>[39]</sup> reported almost full density (99 pct  $\rho_{th}$ ) for mechanically alloyed Cu-5Cr after using a combination of hot pressing (900 °C, 1 hour) and extrusion process (600 °C). In another work, Sharma *et al.*<sup>[40]</sup> processed Cu-10Pb *via* spark plasma sintering technique at 350 °C under 100 MPa pressure for 5 minutes. They could achieve a maximum relative density of ~ 90 pct  $\rho_{th}$ . Nassef *et al.*<sup>[41]</sup> studied the use of Pb, C in densifying Cu-Sn alloys, which were hot-pressed at 550 °C, 314 MPa for 30 minutes. A very low density of 78, 74, and 72 pct  $\rho_{th}$  were reported for Cu-50Ni, Cu-50Zr, and Cu-10Ni-40Zr alloys, respectively, which were processed considerably at a low hot press temperature of 300 °C and high pressure of 900 MPa.<sup>[42]</sup> From the above discussion, it can be understood that higher densification of Cu-based alloys is possible by careful selection of sintering conditions. The present work clearly indicates the advantage of using the high hot

press pressure to achieve higher densities (~ 95 to 96 pct  $\rho_{th}$ ) of Cu-Al alloys at a relatively low sintering temperature of 500 °C and application of high pressure of 500 MPa for 30 minutes. It is a promising result as the overall processing costs in developing Cu-based materials can be reduced. In most commonly used conventional processes, use of high temperature and low-pressure sintering conditions result in coarser grain structure and poor mechanical properties. Hence, additional heat treatment processes or mechanical working methods need to be adopted to improve materials properties further. High-temperature processes or additional processing steps add up the cost as well.

To understand the effect of milling and hot press on densification of Cu-Al alloys, the dislocation density is evaluated from the Williamson–Hall (W–H) model<sup>[43,44]</sup> that is based on the crystallite size (*d*) determination. The W–H model plots obtained from the X-ray diffraction patterns of milled powders as well as sintered compacts are presented in Figure 9 for estimating the dislocation density and lattice strains.

According to Williamson–Hall model, the lattice strain of Cu-Al powders after planetary ball milling process was calculated to be in the range between  $0.31 \times 10^{-2}$  and  $0.62 \times 10^{-2}$ , whereas the lattice strain for hot-pressed samples estimated in the range of  $0.22 \times 10^{-2}$  to  $0.36 \times 10^{-2}$ . It was observed that the lattice strain of milled powders and the hot-pressed Cu



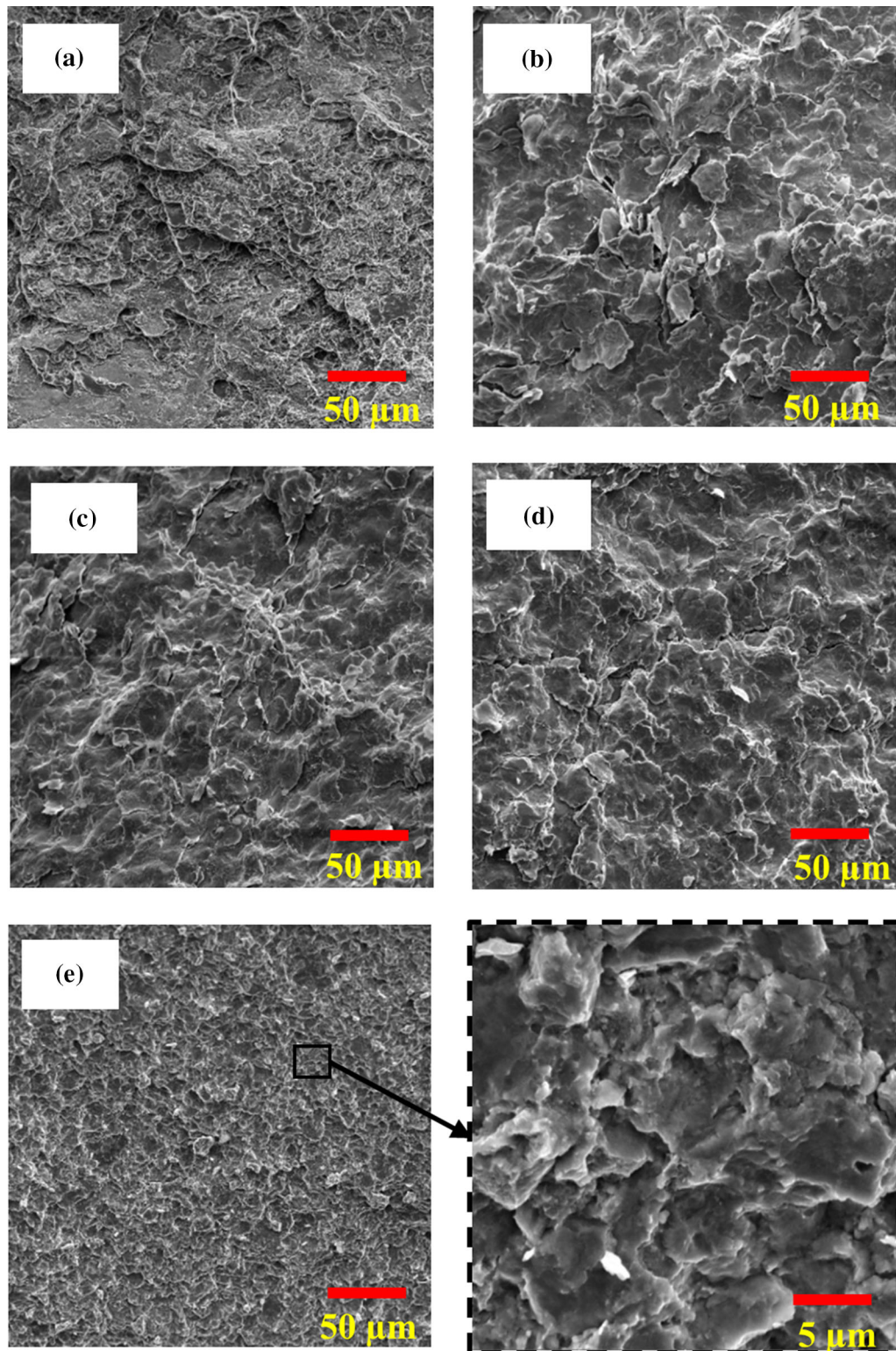


Fig. 7—Fracture surfaces of Cu-Al hot-pressed (at 500 °C, 500 MPa, 30 min under vacuum) samples. (a) Cu, (b) Cu-3Al, (c) Cu-5Al, (d) Cu-10Al, (e) Cu-15Al, and the magnified image of Cu-15Al is shown for acumen. All the samples are characterized with the mixed (intergranular and transgranular) mode of fracture.

samples increased with the addition of Al content and is mainly due to mechanical alloying and formation of solid solutions ( $\alpha$ -Cu) and  $\gamma_2$  intermetallic compound. According to Eqs. [4] and [5],<sup>[45]</sup> Bragg angle ( $\theta$ ),

radiation wavelength ( $\lambda = 1.54056 \text{ \AA}$  for Cu-K $\alpha$  radiation), geometric constant ( $\kappa = 0.94$ ),<sup>[43,46]</sup> and full-width at half maximum ( $B(2\theta)$ ) are related to dislocation density ( $\delta$ ) and crystallite size ( $d$ ). The dislocation



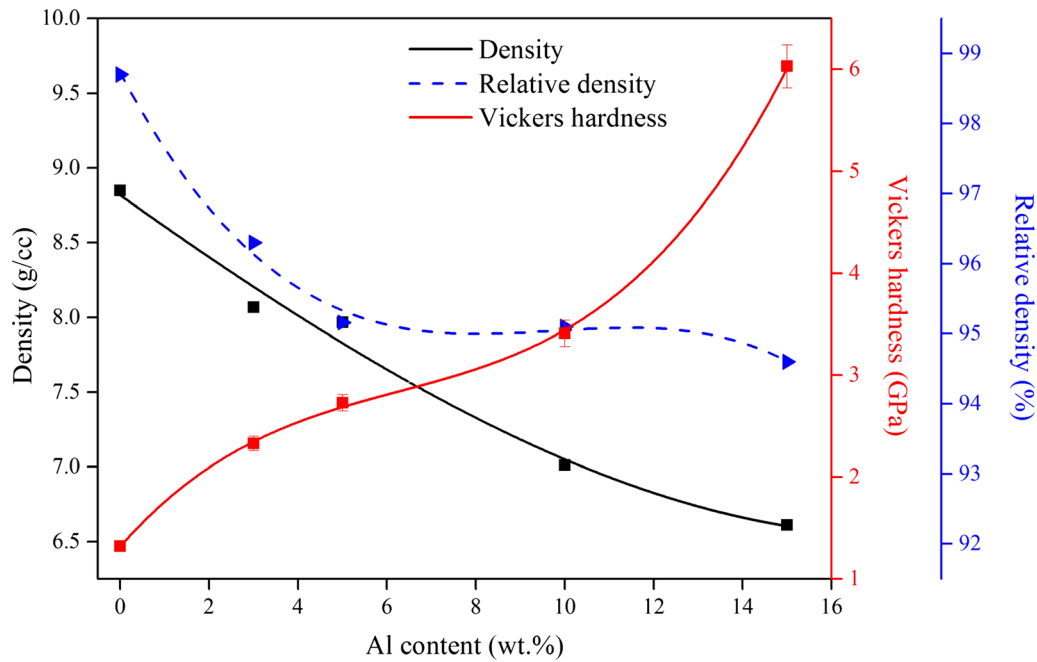


Fig. 8—Effect of Al content on the density and hardness of Cu-Al alloys after hot pressing at 500 °C, 500 MPa pressure for 30 min under vacuum.

density ( $\delta$ ) of milled powders was calculated using the Williamson–Hall model and it varied from  $3.52 \times 10^{14}$  to  $14.61 \times 10^{14} \text{ m}^{-2}$ . Also, the dislocation density of hot-pressed compacts was calculated to be in the range of  $0.63 \times 10^{14}$  to  $4.08 \times 10^{14} \text{ m}^{-2}$ . It is obvious that the lattice strain and dislocation density of milled powders are significantly higher than the hot-pressed samples.

$$\delta = \frac{1}{d^2} \quad [4]$$

$$B(2\theta) \cos \theta = \frac{0.9\lambda}{d} + 2^2 e \sin \theta. \quad [5]$$

The intercept and slope data of milled powders and hot-pressed Cu-Al samples which were obtained from W–H methodology are provided in Table III. The slope of the curves has an inverse relation with the crystallite size of milled powders and hot-pressed samples. The crystallite size for Cu decreased for both the milled powders (from 53.33 to 26.16 nm) and hot-pressed materials (from 126.04 to 49.52 nm) with the addition of Al.

The dislocation density of Cu-Al samples after hot pressing decreased when compared to milled powders. The dislocation density might have decreased due to recovery and recrystallization processes of Cu at the hot press temperature. Very high hot press pressure was used, which is probably the reason why the decrease in dislocation density is slightly low after hot press than the milled samples. In case of Cu-Al alloys, the alloying element effects the dislocation density by forming the solid solution phases ( $\alpha$ -Cu) and intermetallic compounds ( $\gamma_2$ ); as the amount of Al content increased up to

15 wt pct, the dislocation density increased by 6.47 times. The calculated dislocation density using the Williamson–Hall model in milled Cu-Al powders and hot-pressed Cu-Al compacts is listed in Table IV. The crystallite size of both milled powders and hot-pressed samples decreased with the Al content due to the formation of solid solutions. It lowers the ductility in powder particles during the milling process, where the particles get fractured and re-welded with hard agglomerate formation. During hot pressing at 500 °C, the samples exposed to high activation energy which increases the crystallite size of Cu. Thus, the crystallite size of hot-pressed samples is high when compared to milled powders. It was observed that the micro-strain of Cu-Al powders and hot-pressed compacts directly relates to the dislocation density. With the addition of 15 wt pct Al to Cu, a maximum micro-strain of 0.63 pct was calculated for milled powders, whereas the hot-pressed samples were having the maximum strain of 0.36 pct.

Rohatgi *et al.*<sup>[47]</sup> studied the behavior of cold working on Cu-Al alloys by varying the pressure. They estimated the dislocation density of Cu-Al alloys from the DSC curve, *i.e.*, by calculating the energy released during recrystallization. It was reported that the dislocation density of Cu-4Al increased from  $1.22 \times 10^{14}$  to  $17.64 \times 10^{14} \text{ m}^{-2}$  by increasing pressure from 10 to 35 GPa. Zhao *et al.*<sup>[48]</sup> reported the dislocation density of  $2.3 \times 10^{14} \text{ m}^{-2}$  for ultra-fine copper and  $5.9 \times 10^{14} \text{ m}^{-2}$  for ultra-fine bronze that was processed by high-pressure torsion (HPT) at 6 GPa pressure and cold rolling. In another study, the dislocation density of  $4.3 \times 10^{14} \text{ m}^{-2}$  was reported for Equal Channel Angular Pressing (ECAP)-processed copper.<sup>[49]</sup> From these studies, it can be observed that the dislocation density of

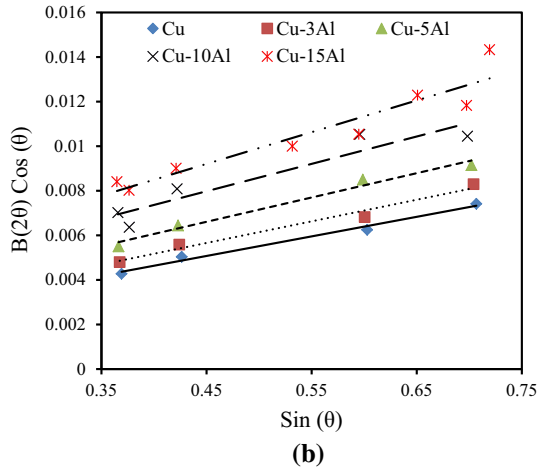
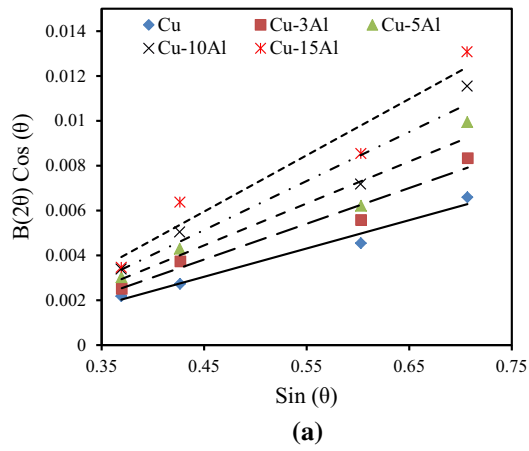


Fig. 9—Williamson–Hall plot obtained from the X-ray diffraction patterns of (a) planetary ball-milled powders, (b) hot-pressed Cu-Al alloys. (Hot pressing conditions: Temperature: 500 °C, Pressure: 500 MPa, Time: 30 min under Vacuum environment).

**Table III. W–H Plot Linear Fit Results of Cu-Al Milled Powders and Hot-Pressed Compacts**

Sample Reference	Milled Powders		Hot-Pressed Compacts	
	Slope ( $\times 10^{-2}$ )	Intercept ( $\times 10^{-3}$ )	Slope ( $\times 10^{-2}$ )	Intercept ( $\times 10^{-3}$ )
Cu	1.26	2.6	0.88	1.1
Cu-3Al	1.59	3.4	0.97	1.3
Cu-5Al	1.87	4.0	1.09	1.7
Cu-10Al	2.19	4.7	1.23	2.4
Cu-15Al	2.51	5.3	1.42	2.8

Cu-based alloys is varying with the function of temperature and pressure, *i.e.*, the dislocation density of Cu alloys was observed to be low at the higher processing temperature and lower pressures. Also, the calculated dislocation density values of Cu-Al alloys in the present study are comparable with the reported Cu alloys.

In summary, the dislocation density and lattice strain enhances the densification and densification rate of Cu-Al samples. For example, as it was reported, Rajkovic *et al.*<sup>[38]</sup> could only achieve a maximum

density of 85.1 pct  $\rho_{th}$  for hot-pressed Cu-3.5Al even after using high sintering temperature of 800 °C and the pressure of 35 MPa for 1 hour. Whereas in the present work, we observed a maximum density of 96.3 pct  $\rho_{th}$  for Cu-3Al after hot press at a low temperature of 500 °C and the pressure of 500 MPa for 30 minutes. In case of pure Cu, a very high density of 98.66 pct  $\rho_{th}$  could be achieved under similar processing conditions.

### C. Microhardness of Cu-Al Alloys

The hardness of Cu increased with the amount of Al; in particular, Cu-15Al alloy exhibited a significantly high hardness of 6.03 GPa when compared to pure Cu (1.32 GPa) (see Figure 8). It also to be noted here that the hardness measured for pure copper in the current study is relatively high than reported values of Cu (in the literature) and it can be attributed to its high density and fine structure. The Cu-Al alloys with low Al content (preferably Cu-3Al and Cu-5Al) that consist of  $\alpha$ -Cu solid solution phase exhibited high hardness in the range of 2.33 to 2.73 GPa (almost two times of Cu). Such high harness of these alloys is due to solid solution strengthening. However, in the presence of  $\gamma_2$  intermetallic phase along with  $\alpha$  solid solution in Cu-10Al and Cu-15Al, the hardness of these alloys is measured to be much high and varied between 3.41 and 6.03 GPa. This improvement in hardness of Cu-Al alloys can be attributed to the reduction of grain size, solid solution strengthening, and intermetallic phase formation. Liu *et al.*<sup>[50]</sup> reported low Vickers hardness (2.00 to 2.75 GPa) for Cu-*x*Al (*x*: 1, 2, 4, and 6) alloys which were processed by arc melting technique (at a temperature range between 710 °C and 800 °C). In another work, Glas<sup>[51]</sup> reported hardness of 2.95 to 3.7 GPa for Cu-Al alloys processed by casting technique (at 1150 °C). Also, Nassef *et al.*<sup>[41]</sup> produced the Cu-Sn and Cu-Pb alloys through hot pressing route; depending on the composition the hardness of Cu-10Pb alloys varied between 1.01 and 2.10 GPa, whereas for Cu-10Sn-10Pb it varied between 1.08 and 2.22 GPa. So far in the literature, for Cu-based materials a maximum hardness of 4.1 GPa was reported;<sup>[6,41,52,53]</sup> however, in the present work, very high hardness of 6.03 GPa was achieved for hot-pressed Cu-Al alloys.

### D. Nano-indentation Behavior

The nanohardness and elastic modulus of hot-pressed Cu-Al alloys were determined from the loading and unloading curves using the method proposed by Oliver–Pharr.<sup>[54,55]</sup>

Figure 10(a) shows an optical microscopic representative image of nano-indentations taken on the Cu-15Al alloy with an array of 10  $\times$  10 size with 40- $\mu$ m indent spacing. From Figures 10(b) through (f), the indentation size of the pure copper sample was measured to be  $3.75 \pm 0.1 \mu\text{m}$ ; the indentation size of Cu was reduced to  $1.98 \pm 0.08 \mu\text{m}$  as the Al content added up to 15 wt pct. The schematic of the typical load-displacement curve of nano-indentation for viscoelastic-plastic materials is shown in Figure 11(a), where  $h_{max}$



**Table IV. Calculated Dislocation Density Using Williamsons–Hall Model in Milled Cu–Al Powders (After Planetary Ball Milling at 260 rpm for 10 h) and Hot-Pressed Cu–Al Alloys (After Hot Pressing at 500 °C, 500 MPa for 30 min)**

Sample Reference	Milled Powders			Hot-Pressed Compacts		
	Crystallite Size, $L$ (nm)	Micro-strain, $e$ (Pct)	Dislocation Density ( $\times 10^{14} \text{ m}^{-2}$ )	Crystallite Size, $L$ (nm)	Micro-Strain, $e$ (Pct)	Dislocation Density ( $\times 10^{14} \text{ m}^{-2}$ )
Cu	53.33	0.32	3.52	126.04	0.22	0.63
Cu-3Al	40.78	0.40	6.01	106.65	0.24	0.88
Cu-5Al	34.66	0.47	8.32	81.56	0.27	1.50
Cu-10Al	29.50	0.55	11.49	57.77	0.31	3.00
Cu-15Al	26.16	0.63	14.61	49.52	0.36	4.08

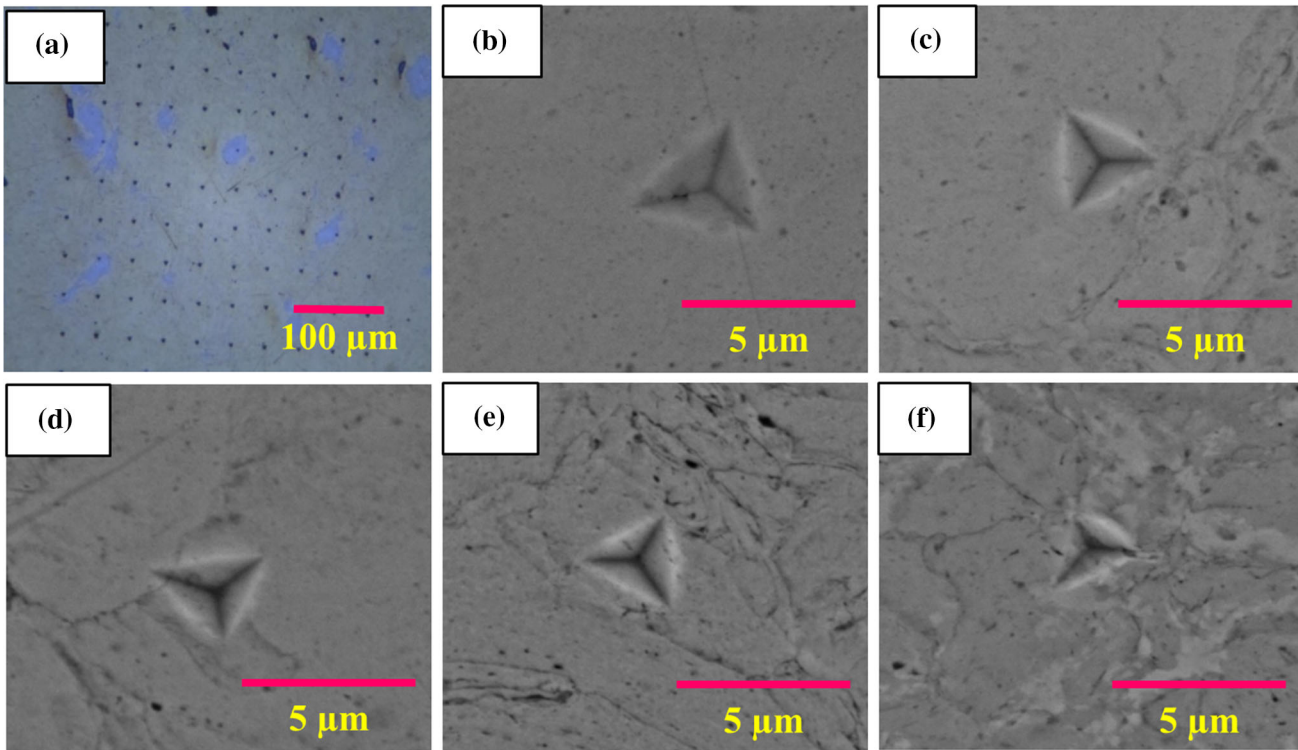


Fig. 10—SEM image showing typical nano-indentations obtained on hot-pressed Cu–Al alloys. (a) Optical microscopic image Cu-10Al alloy having the array of 100 indentations and corresponding indents of (b) Cu, (c) Cu-3Al, (d) Cu-5Al, (e) Cu-10Al, and (f) Cu-15Al.

represents the maximum displacement of indenter at peak load ( $P_{\max}$ ),  $h_f$  is the depth of residual impression after unloading, and  $h_c$  is the contact depth under the indenter. The elastic modulus ( $E_s$ ) of hot-pressed samples was calculated using Eq. [6], where the reduced modulus ( $E_r$ ) obtained directly from the nano-indentation system and the Poisson's ratio ( $\nu$ ) of the Cu–Al alloys, which was taken to be 0.3, indenter elastic modulus ( $E_i$ )  $\sim 1141$  GPa, and its Poisson's ratio ( $\nu$ )  $\sim 0.07$ .<sup>[56]</sup>

$$\frac{1}{E_r} = \frac{(1 - \nu_s^2)}{E_s} + \frac{(1 - \nu_i^2)}{E_i}. \quad [6]$$

The loading–unloading curves of hot-pressed samples obtained at a constant peak load of 20 mN and the loading–unloading rate of 2 mN/s are presented in

Figure 11(b). It is clear from the loading–unloading curves that the Al content has a significant effect on the indentation behavior of Cu–Al hot-pressed samples. The presence of plateau, which indicates the creep of Cu–Al alloys, can be seen in Figure 11(b). It was evident that the length of the plateau is small for Cu-10Al and Cu-15Al when compared to other Cu materials. In particular, pure Cu witnessed with the maximum plateau. It indicates that the creep deformation of Cu-10Al and Cu-15Al alloys is considerably low than the other alloys. The indentation depth decreased with the increase of Al in Cu–Al alloys. The indentation depth of the pure copper was measured as  $\sim 576$  nm, whereas for the Cu-15Al it reduced to  $\sim 324$  nm. The average nano-indentation hardness ( $H$ ) of Cu–Al alloys increased considerably from  $2.38 \pm 0.18$  to  $7.88 \pm 0.98$  GPa.

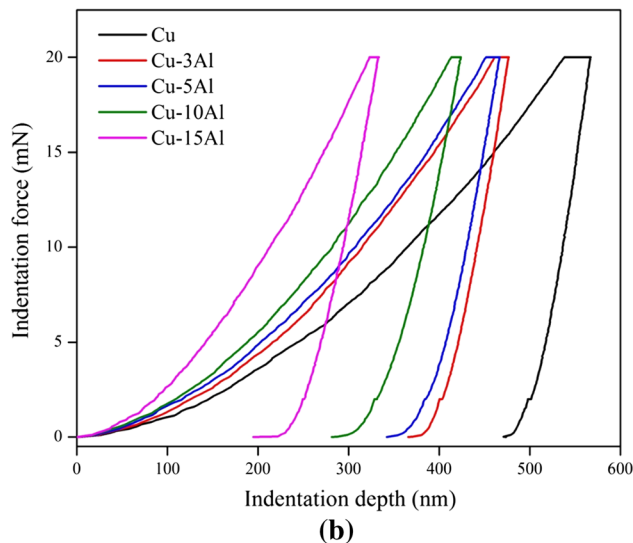
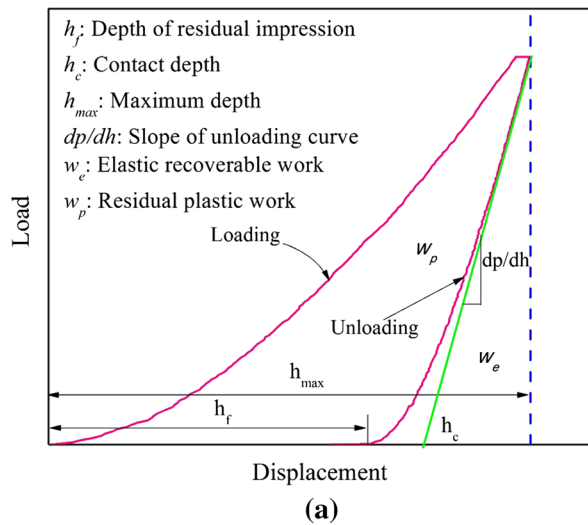


Fig. 11—(a) Schematic of typical load ( $P$ )–displacement ( $h$ ) curve of nano-indentation for viscoelastic-plastic materials, (b) indentation load vs penetration depth curves of Cu–Al alloys at an indent peak load of 20 mN (loading and unloading rate: 2.0 mN/s).

The nanohardness represents materials resistance to deformation. The improved nanohardness of Cu–Al alloys reflects the deformation resistance of these alloys with Al content. From the unloading portion of the load–depth curves, the elastic modulus ( $E$ ) of hot-pressed samples was calculated and found to be increased from  $123.18 \pm 4.6$  to  $177.35 \pm 9.6$  GPa (see Figure 12). The mechanical properties of Cu–Al alloys evaluated from the nano-indentation test are listed in Table V. In the literature, it was reported that the ratio of hardness ( $H$ ) to elastic modulus ( $E$ ) has a relation with wear resistance.<sup>[24]</sup> The higher the  $H/E$  ratio, the higher will be the wear resistance. As it is shown in Table V, the  $H/E$  ratio of Cu increases with Al and the  $H/E$  ratio increases from 0.019 for pure Cu to 0.044 for Cu–15Al.

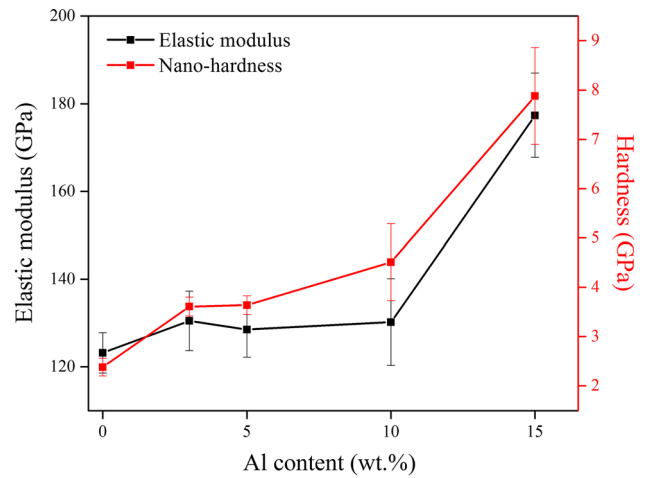


Fig. 12—The effect of Al content on elastic modulus and hardness of Cu–Al alloys measured from the  $P$ – $h$  plots of nano-indentation.

Based on the literature, the mechanical properties of various Cu alloys obtained by the nano-indentation test are summarized in Table VI. Most of the nano-indentation studies were made for Cu alloy coatings. The nanohardness of Cu alloys reportedly varied between 3.38 and 6.50 GPa and the elastic modulus varied from 100 to 170 GPa.<sup>[24,57–63]</sup>

The plastic deformation and its behavior of hot-pressed samples under nano-indentation can be understood by using the plasticity index ( $\psi$ ) parameter.<sup>[64,65]</sup> From the load vs indenter penetration depth curves, recovered elastic work ( $W_e$ ) and residual plastic work ( $W_p$ ) can be measured by integrating the area under unloading curve and the area between loading–unloading curves, respectively.<sup>[66]</sup> The plasticity index of the hot-pressed samples can be calculated by using the Eq. [7]. The elastic recoverable work, residual plastic work, and plasticity index of hot-pressed samples calculated from the load–displacement curves are given in Table VII.

$$\psi = \frac{W_p}{W_t} \quad [7]$$

The plasticity index of the Cu–Al alloys was found to be reduced as the Al content increases; for the pure copper, it was estimated to be 0.85, whereas for Cu–15Al alloy ~ 0.66. The reduction in plasticity index of the Cu–15Al alloy is 22.5 pct when compared to pure copper. This is indicating that the Cu–Al alloys still retain a significant amount of plasticity under indentation conditions. The distribution of hardness of Cu–Al alloys is presented in Figure 13. The nanohardness of Cu–Al alloys varied between 2.38 and 7.88 GPa; nevertheless, Cu–15Al exhibited maximum hardness. The scattering in hardness of Cu–Al alloys can be attributed to its microstructure. In the case of Cu and Cu alloys up to 5 wt pct Al, the hardness is almost uniformly/narrowly distributed due to its single phase. There is a wide deviation or scatter in the hardness of Cu–10Al and Cu–15Al as they consisted of two different phases. The



**Table V. Mechanical Properties of Cu-Al Alloys Based on the Nano-indentation Test**

Sample Reference	Hardness ( $H$ ) (GPa)	Reduced Modulus ( $E_r$ ) (GPa)	Elastic Modulus ( $E$ ) (GPa)	$H/E$	Maximum displacement ( $h_{max}$ ) (nm)
Cu	$2.38 \pm 0.18$	$121.07 \pm 4.0$	$123.18 \pm 4.6$	0.019	565
Cu-3Al	$3.61 \pm 0.19$	$127.44 \pm 3.6$	$130.47 \pm 6.3$	0.027	476
Cu-5Al	$3.64 \pm 0.19$	$125.72 \pm 3.4$	$128.49 \pm 6.3$	0.028	465
Cu-10Al	$4.51 \pm 0.78$	$129.19 \pm 7.5$	$135.18 \pm 9.9$	0.033	423
Cu-15Al	$7.88 \pm 0.98$	$166.58 \pm 6.2$	$177.35 \pm 9.6$	0.044	324

**Table VI. Nano-indentation Properties of Various Cu Alloys Reported in the Literature**

Alloy	Manufacturing Process	Nano-indentation Test Conditions	Hardness ( $H$ ) (GPa)	Elastic Modulus ( $E$ ) (GPa)	Maximum Displacement ( $h_{max}$ ) (nm)	Ref.
Cu-22Al	as casting	$I$ : Berkovich, $l$ : 1 mN $v$ : $100 \mu\text{N s}^{-1}$	3.5	112.27	102.56	24
Cu-11.76Al	as casting + annealed at 500 °C, 15 min	$I$ : Berkovich, $l$ : 10 nN $v$ : $100 \mu\text{N s}^{-1}$	3.38	111.87	105.65	57
Cu-11.76Al	cryogenic treated at -196 °C, 30 min	$I$ : Berkovich, $l$ : 10 nN $v$ : $100 \mu\text{N s}^{-1}$	3.67	115.35	94.62	57
Cu-11.2Al-6.9Fe	plasma transferred arc welding deposition	$I$ : Berkovich, $d$ : 500 nm	4.9	121.7	500	58
Cu-Al*	hot pressing, 350 °C to 650 °C, 10 min	$I$ : Berkovich, $d$ : 150 nm	$6.06 \pm 0.18$	—	—	59
Cu-11Ni-1P	annealed at 500 °C, 2 h	$I$ : Berkovich, $d$ : 1000 nm	3.6	—	1010	60
Cu-11Ni-1P	electrodeposition	$I$ : Berkovich, $d$ : 1000 nm	5.2	—	1025	60
Cu-Sn*	solid-state aging + annealing at 200 °C, 341 h	$I$ : Berkovich, $l$ : 0.7 to 9.5 mN $v$ : $1 \text{ mN s}^{-1}$	$6.5 \pm 0.3$	$128 \pm 10$	98	61
Cu-6.5at. pctTi	magnetron sputtering deposition	$I$ : Berkovich, $l$ : 2.6 mN $v$ : $0.01 \text{ nN s}^{-1}$	$\sim 4.9$	—	130	62
Cu-8at. pctMo	magnetron sputtering deposition	$I$ : Berkovich, $l$ : 2.6 mN $v$ : $0.01 \text{ nN s}^{-1}$	$\sim 5.0$	—	155	62
Cu-30Ag	thermal deposition	$I$ : Berkovich, $d$ : 80 nm	4.0	100 to 170	$\sim 800$	63

\*Diffusion bonding,  $I$ : type of indenter,  $l$ : load,  $v$ : loading/unloading speed,  $d$ : depth.

**Table VII. Elastic Recoverable Work, Residual Plastic Work, and Plasticity Index of Cu-Al Alloys**

Sample Reference	Elastic Recoverable Work ( $W_e$ ) ( $\times 10^{-6}$ J)	Residual Plastic Work ( $W_p$ ) ( $\times 10^{-6}$ J)	Plasticity Index ( $\psi$ )
Cu	0.662	3.792	0.85
Cu-3Al	0.750	2.837	0.79
Cu-5Al	0.810	2.757	0.77
Cu-10Al	0.917	2.284	0.71
Cu-15Al	0.858	1.735	0.66

cumulative values of the hardness of Cu-Al alloys are shown in Figure 14.

The cumulative hardness of Cu-Al alloys shows the pop-in effect which is associated with phase variations or microstructure and correspondingly represents hardness. In pure copper, no pop-in effect has been observed as it does not have any phase change. The pop-in effect was not observed for pure Cu, Cu-3Al, and Cu-5Al alloys as their microstructure consists of a single phase. On the other hand, the pop-in was found at 4.7 GPa corresponding to the hardness of the  $\alpha$  phase in the Cu-10 Al alloy. The Cu-15Al alloy shows different pop-in effects,<sup>[67]</sup> which indicates the broad range of hardness regarding  $\alpha$  and  $\gamma_2$  phases.

### E. Compression Behavior

Figure 15 shows the compression stress–strain curves of Cu-Al alloys. From Figure 15(a), it can be observed that the compressive strength of Cu-Al alloys increased significantly and the compressive strain decreased with Al addition. The compression properties of Cu-Al alloys are presented in Table VIII.

The compressive strength of Cu increased from  $813.75 \pm 11$  to  $1120.18 \pm 28$  MPa with the addition of Al. However, the compressive strain reduced from  $29.81 \pm 0.9$  to  $5.81 \pm 0.3$  pct (see Figure 15(c)). From Figure 15(b), a common observation is that a significant high compressive strength of  $1120.18 \pm 28$  MPa is

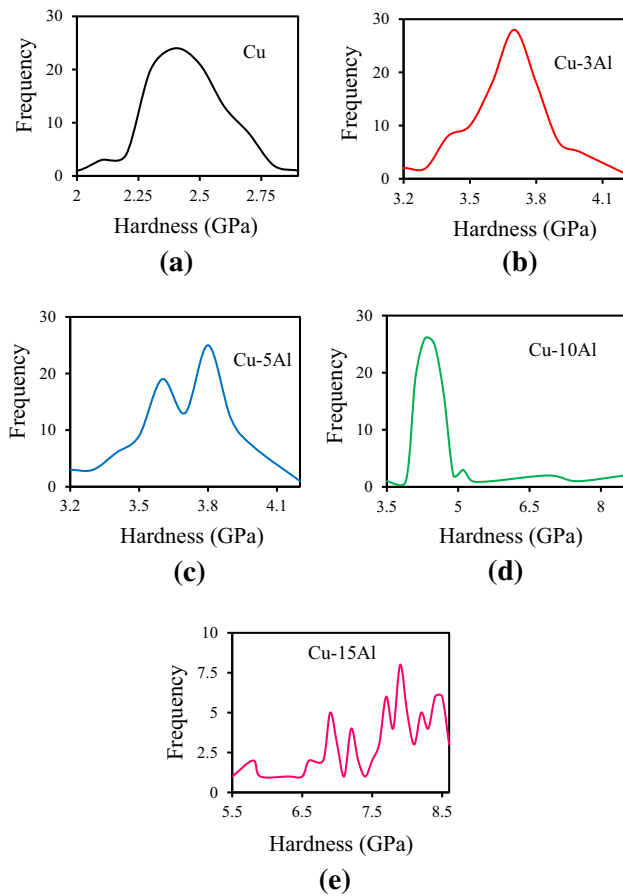


Fig. 13—Distribution of nanohardness at various phases of Cu-Al alloys plotted from load vs penetration depth curves at an indent peak load of 20 mN (loading and unloading rate: 2.0 mN/s) (a) through (e).

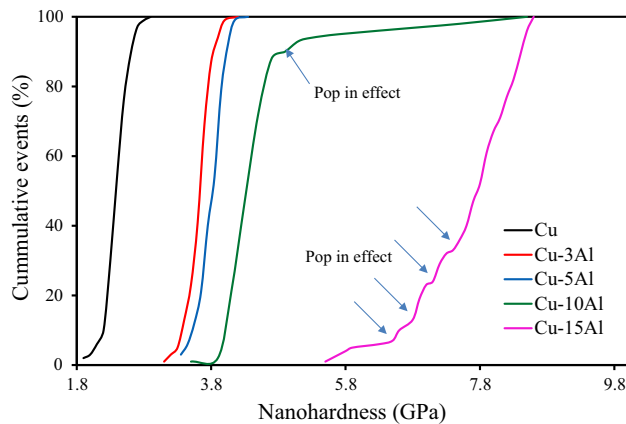


Fig. 14—Cumulative events (pct) of nanohardness of Cu-Al alloys. The pop-in effect shows the presence of different phases.

achieved for Cu-5Al with a reasonable amount of strain ( $8.0 \pm 0.7$  pct).

Since the Cu-5Al alloy has the major constituent of  $\alpha$ -Cu and the combined features of a microstructure such as finer and elongated grains might have contributed to its good combination of properties. Due to

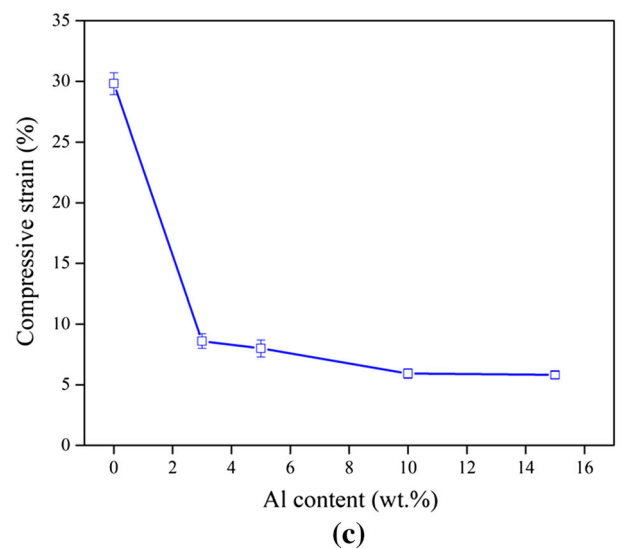
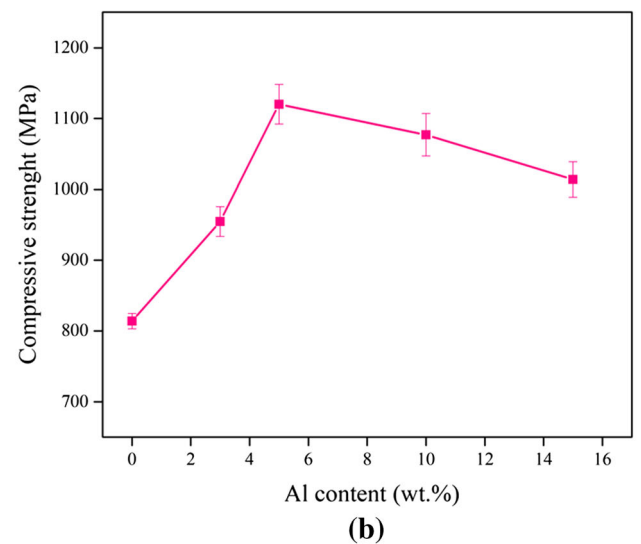
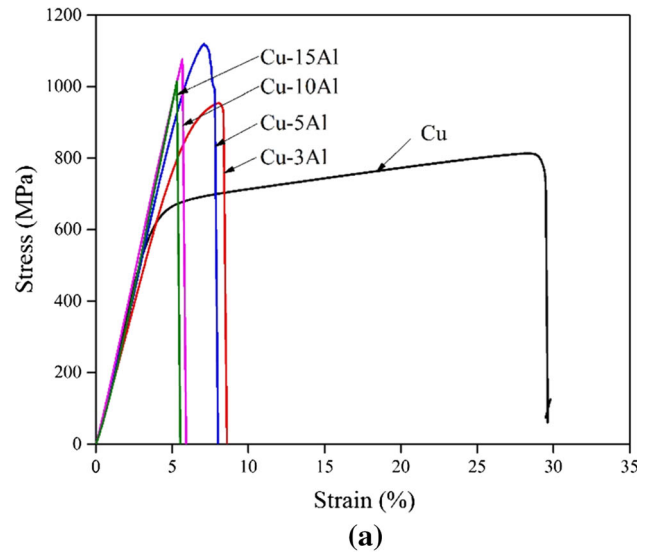


Fig. 15—(a) Compression stress-strain curves of Cu-Al alloys, effect of Al on (b) compressive strength and (c) compressive strain of Cu.



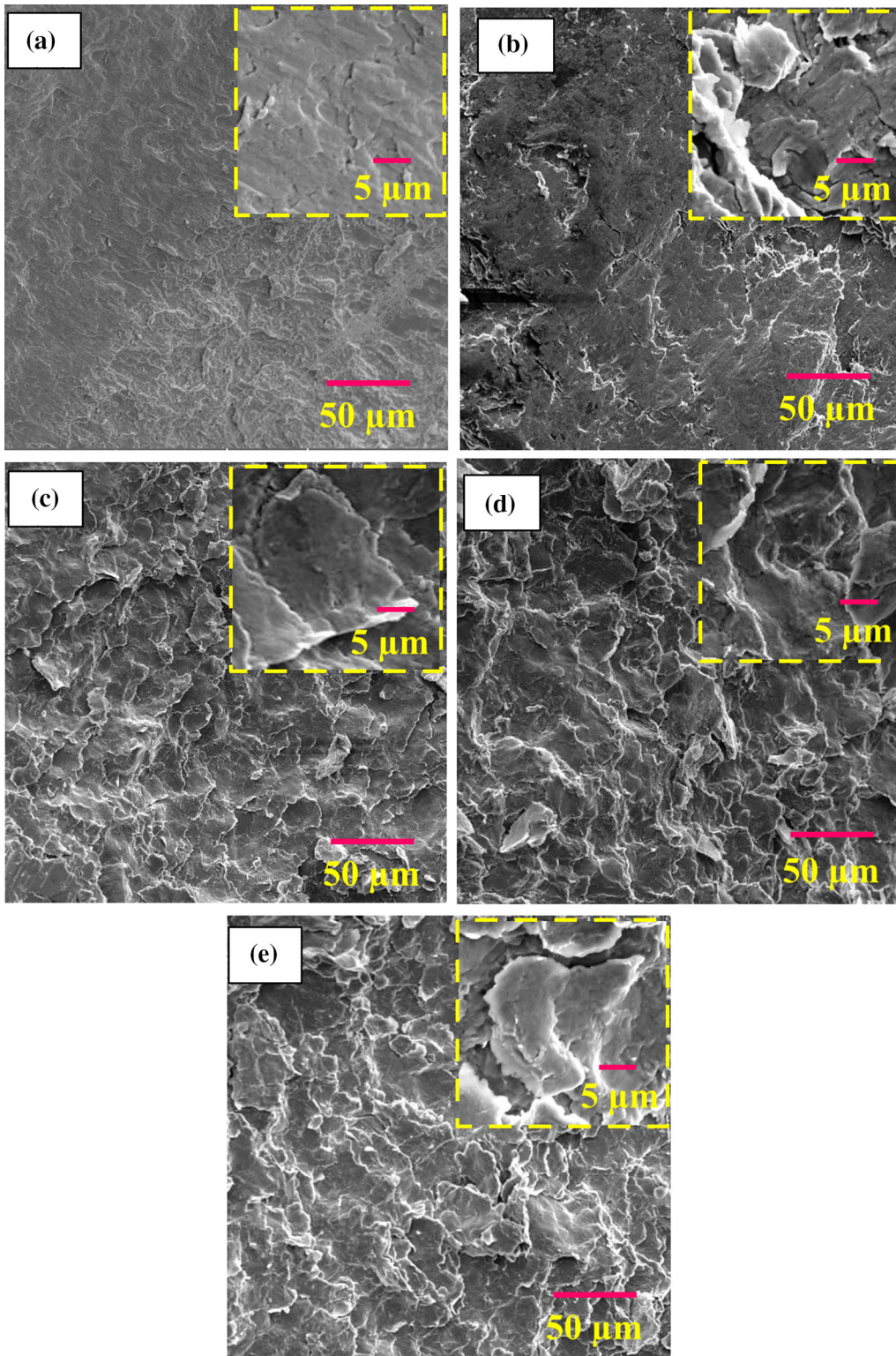


Fig. 16—Fractured surfaces of compression tested Cu-Al alloys (Hot press conditions: 500 °C, 500 MPa for 30 min). (a) Cu, (b) Cu-3Al, (c) Cu-5Al, (d) Cu-10Al, and (e) Cu-15Al. The insets represent high-magnification images.

the formation intermetallic phase ( $\gamma_2$ ) and rich solid solution phase in Cu-10Al alloys, its strength ( $1077 \pm 30$  MPa) lowered when compared to Cu-5Al alloy. The similar kind of behavior was observed in the case of Cu-15Al, which is having the compressive

strength of  $1077.05 \pm 30$  MPa with a moderate compressive strain of  $5.81 \pm 0.3$ .

The fractured surfaces of pure copper and Cu-Al alloys after the compression test are presented in Figure 16. During the compression test, the Cu-Al

**Table VIII. Compression Test Results of Cu-Al Alloys**

Sample Reference	Compressive Strength (MPa)	Elongation (Pct)
Cu	813.75 ± 11	29.81 ± 0.9
Cu-3Al	954.71 ± 21	8.61 ± 0.6
Cu-5Al	1120.18 ± 28	8.00 ± 0.7
Cu-10Al	1077.05 ± 30	5.93 ± 0.4
Cu-15Al	1013.82 ± 25	5.81 ± 0.3

alloys showed an inclined fracture surface, about 45 deg with the applied load axis, which is a similar failure criterion of hard materials.<sup>[68]</sup> The change in strength behavior of Cu-Al alloys is mainly because of the change in the mode of fracture. In fact, in Cu with up to 5 wt pct Al, the fracture mode is predominantly of transgranular and it changed to more of intergranular with further addition of Al to Cu (Figure 16).

In view of its good sliding wear properties, aluminum bronzes have been used as tool material in sheet metal forming of stainless steel, which is used for the production of washing, refrigeration, and cooking equipment.<sup>[69]</sup> It was reported that the tool wear of these alloys was sensitive to its limited hardness. In this context, achieving the high hardness and good compression strength of Cu-Al alloys is very promising.

#### IV. CONCLUSIONS

1. The density of Cu- $X$  wt pct Al ( $X = 0, 3, 5, 10, 15$ ) alloys varied between 95 and 98 pct  $\rho_{th}$  after subjecting the mechanically alloyed powders at a hot pressing temperature of 500 °C and 500 MPa pressure for 30 minutes under a vacuum environment. The measured experimental/bulk density of samples varied between 8.84 and 6.61 g/cc.
2. According to Williamson–Hall model, the lattice strain of Cu-Al powders after ball milling process was calculated to be in the range between  $0.31 \times 10^{-2}$  and  $0.62 \times 10^{-2}$ , whereas the lattice strain of hot-pressed samples was in the range of  $0.22 \times 10^{-2}$  to  $0.36 \times 10^{-2}$ . The crystallite size for Cu decreased for both the milled powders (from 53.33 to 26.16 nm) and hot-pressed materials (from 126.04 to 49.52 nm) with the addition of Al.
3. The dislocation density of milled powders calculated using the Williamson–Hall model varied from  $3.52 \times 10^{14}$  to  $14.61 \times 10^{14} \text{ m}^{-2}$ . Also, the dislocation density of hot-pressed compacts varied in the range of  $0.63 \times 10^{14}$  to  $4.08 \times 10^{14} \text{ m}^{-2}$ .
4. The XRD and SEM-EDS analyses of hot-pressed samples confirm the formation of  $\alpha\text{Cu}$  solid solution phase ( $\text{Cu}_{0.92}\text{Al}_{0.08}$ ) for Cu alloyed with Al (up to 5 wt pct). Further addition of Al leads to the formation of aluminum-rich  $\alpha\text{Cu}$  solid solution phase ( $\text{Cu}_{0.78}\text{Al}_{0.22}$ ) and an intermetallic compound ( $\text{Cu}_9\text{Al}_4$ ) in Cu-Al alloys.
5. The nano-indentation tests revealed an increase of hardness (2.4 to 7.9 GPa) and elastic modulus

(121.1 to 177.4 GPa) and decreases in the plasticity of the index (0.85 to 0.66) for Cu-Al alloys with increasing Al content. Solid solution strengthening, intermetallic compound presence, good densification, and fine microstructure of Cu-Al alloys can be attributed to such better properties.

6. The compressive strength of Cu increased (from 813.75 to 1120.18 MPa) significantly and the compressive strain decreased (from 29.81 to 5.81 pct) with the addition of Al.
7. A comparison of mechanical properties of presently developed Cu-Al hot-pressed alloys with the existing literature clearly indicated that the presently developed alloys exhibited superior mechanical properties. It is very obvious that use of low hot press sintering temperature with high pressure is effective in achieving good mechanical properties of Cu-Al alloys.

#### FUNDING

Ministry of Human Resource and Development, Government of India is gratefully acknowledged for the financial support to procure hot press equipment under plan grants (Departmental Plan-Grant Funds Code No: P828) that is used in the present work.

#### CONFLICT OF INTEREST

The authors declare that they have no conflict of interest.

#### REFERENCES

1. H. Jang, K. Ko, S.J. Kim, R.H. Basch, and J.W. Fash: *Wear*, 2004, vol. 256, pp. 406–14.
2. H.M. Zaw, J.Y.H. Fuh, A.Y.C. Nee, and L. Lu: *J. Mater. Process. Technol.*, 1999, vol. 89, pp. 182–86.
3. D. Prokoshkina, V.A. Esin, and S.V. Divinski: *Acta Mater.*, 2017, vol. 133, pp. 240–46.
4. M. Rabiee, H. Mirzadeh, and A. Ataie: *J. Ultrafine Grained Nanostruct. Mater.*, 2016, vol. 49, pp. 17–21.
5. A. Heidarzadeh and T. Saeid: *Rare Met.*, 2016, vol. 35, pp. 1–11.
6. A.E. Nassef, A.I. Alateyah, M.A. El-Hadek, and W.H. El-Garaihy: *Adv. Mater. Lett.*, 2017, vol. 8, pp. 717–22.
7. G.S. Jawaharram, S.J. Dillon, and R.S. Averback: *J. Mater. Res.*, 2017, vol. 32, pp. 3156–64.
8. J. Guo, J. Rosalie, R. Pippin, and Z. Zhang: *Scripta Mater.*, 2017, vol. 133, pp. 41–44.
9. J.R. Davis and A.S.M.I.H. Committee: *Copper and Copper Alloys*, ASM International, Cleveland, 2001.
10. A. Korneva, B. Straumal, A. Kilmametov, R. Chulist, P. Straumal, and P. Zięba: *Mater. Charact.*, 2016, vol. 114, pp. 151–56.
11. A.T. Vijayashakthivel, T.N. Srikantha Dath, and R. Krishnamurthy: *Proc. Eng.*, 2014, vol. 97, pp. 56–63.
12. M.I. Latypov, E.Y. Yoon, D.J. Lee, R. Kulagin, Y. Beygelzimer, M. Seyed Salehi, and H.S. Kim: *Metall. Mater. Trans. A*, 2014, vol. 45A, pp. 2232–41.
13. S. Tamimi, M. Ketabchi, N. Parvin, M. Sanjari, and A. Lopes: *Int. J. Met.*, 2014, vol. 2014, pp. 1–9.
14. W. Gluchowski, J. Stobrawa, Z. Rdzawski, and W. Malec: *Mater. Sci. Forum*, 2011, vol. 674, pp. 177–88.

15. Y.L. Gong, S.Y. Ren, S.D. Zeng, and X.K. Zhu: *Mater. Sci. Eng. A*, 2016, vol. 659, pp. 165–71.
16. H.S. Park, T. Kimura, T. Murakami, Y. Nagano, K. Nakata, and M. Ushio: *Mater. Sci. Eng. A*, 2004, vol. 371, pp. 160–69.
17. H. Wen, T.D. Topping, D. Isheim, D.N. Seidman, and E.J. Lavernia: *Acta Mater.*, 2013, vol. 61, pp. 2769–82.
18. H. Wen and E.J. Lavernia: *Scripta Mater.*, 2012, vol. 67, pp. 245–48.
19. J.-P. Kruth, P. Peeters, T. Smolderen, J. Bonse, T. Laoui, and L. Froyen: *Rev. Int. CFAO dinformatique Graph.*, 1998, vol. 13, pp. 95–110.
20. J.-P. Kruth, P. Mercelis, J. Van Vaerenbergh, L. Froyen, and M. Rombouts: *Rapid Prototyp. J.*, 2005, vol. 11, pp. 26–36.
21. F.A. Calvo, A. Ureng, J.M.G. De Salazar, and F. Molleda: *J. Mater. Sci.*, 1988, vol. 23, pp. 2273–80.
22. Copper Development Association: *Equilibrium Diagrams the Major Types of Phase Transformation*, 1992.
23. C.Y. Chen and W.S. Hwang: *Mater. Trans.*, 2007, vol. 48, pp. 1938–47.
24. L. Wu, L. Liu, J. Liu, and R. Zhang: *Mater. Trans.*, 2012, vol. 53, pp. 504–07.
25. H.Y. Wang, Y. Chen, Y.W. Liu, F. Li, J.H. Liu, G.-R. Peng, and W.K. Wang: *Chin. Phys. Lett.*, 2009, vol. 26, art. no. 106201.
26. D.S. Zhou, D.L. Zhang, C. Kong, and P. Munroe: *Mater. Sci. Eng. A*, 2013, vol. 584, pp. 67–72.
27. M.F. Giordana, N. Munoz-vasquez, M. Garro-gonzalez, and M.R. Esquivel: *Proc. Mater. Sci.*, 2015, vol. 9, pp. 262–70.
28. R.H. Palma, A.H. Sepúlveda, R.A. Espinoza, and R.C. Montiglio: *J. Mater. Process. Technol.*, 2005, vol. 169, pp. 62–66.
29. F. Wang, Y. Li, K. Yamanaka, K. Wakon, K. Harata, and A. Chiba: *Mater. Des.*, 2014, vol. 64, pp. 441–49.
30. Y. Guo, G. Liu, H. Jin, Z. Shi, and G. Qiao: *J. Mater. Sci.*, 2011, vol. 46, pp. 2467–73.
31. H. Baker: *ASM: Handbook: Vol 3: Alloy Phase Diagrams*, ASM International, Materials Park, OH, 1992.
32. T. Massalski: *Binary Alloy Phase Diagrams*, AIP, Materials Park, OH, 1990.
33. V. Raghavan: *Physical Metallurgy: Principles and Practice*, 3rd ed., Prentice Hall India Pvt., Limited, New Delhi, 2015.
34. I. Cenoz: *Metallurgija*, 2010, vol. 16, pp. 115–22.
35. H.M. Otte: *J. Appl. Phys.*, 1962, vol. 33, pp. 2892–93.
36. J.S. Llewelyn Leach: *J. Inst. Met.*, 1964, vol. 92, pp. 93–94.
37. L. Arnberg and S. Westman: *Acta Crystallogr. Sect. A*, 1978, vol. 34, pp. 399–404.
38. V. Rajkovic, D. Bozic, and M.T. Jovanovic: *Metallurgija*, 2007, vol. 13, pp. 309–16.
39. W. He, E. Wang, L. Hu, Y. Yu, and H. Sun: *J. Mater. Process. Technol.*, 2008, vol. 208, pp. 205–10.
40. A.S. Sharma, K. Biswas, B. Basu, and D. Chakravarty: *Metall. Mater. Trans. A*, 2011, vol. 42A, pp. 2072–84.
41. A. Nassef and M. El-Hadek: *Adv. Mater. Sci. Eng.*, 2016, vol. 53, pp. 38–42.
42. C. Martinez, F. Briones, P. Rojas, S. Ordonez, C. Aguilar, and D. Guzman: *MRS Adv.*, 2017, vol. 2, pp. 2831–36.
43. A. Khorsand Zak, W.H.Abd. Majid, M.E. Abrishami, and R. Yousefi: *Solid State Sci.*, 2011, vol. 13, pp. 251–56.
44. V.D. Mote, Y. Purushotham, and B.N. Dole: *J. Theor. Appl. Phys.*, 2012, vol. 6, art. no. 6.
45. S.F. Varol, G. Babur, G. Cankaya, and U. Kolemen: *RSC Adv.*, 2014, vol. 4, pp. 56645–53.
46. T.D. Shen, R.B. Schwarz, and J.D. Thompson: *Phys. Rev. B*, 2005, vol. 72, art. no. 14431.
47. A. Rohatgi, K.S. Vecchio, and I.G.T. Gray: *Acta Mater.*, 2001, vol. 49, pp. 427–38.
48. Y.H. Zhao, Y.T. Zhu, X.Z. Liao, Z. Horita, and T.G. Langdon: *Appl. Phys. Lett.*, 2006, vol. 89, art. no. 121906.
49. Y.H. Zhao, J.F. Bingert, Y.T. Zhu, X.Z. Liao, R.Z. Valiev, Z. Horita, T.G. Langdon, Y.Z. Zhou, and E.J. Lavernia: *Appl. Phys. Lett.*, 2008, vol. 92, art. no. 81903.
50. G. Liu, J. Gu, S. Ni, Y. Liu, and M. Song: *Mater. Charact.*, 2015, vol. 103, pp. 107–19.
51. F. Glas: *Tribol. Schmier.*, 2005, vol. 52, pp. 55–63.
52. K. Biswas, A.S. Sharma, and B. Basu: *Scripta Mater.*, 2013, vol. 69, pp. 122–26.
53. B.K. Prasad: *Metall. Mater. Trans. A*, 1997, vol. 28A, pp. 809–15.
54. W.C. Oliver and G.M. Pharr: *J. Mater. Res.*, 1992, vol. 7, pp. 1564–83.
55. R. Saha and W.D. Nix: *Acta Mater.*, 2002, vol. 50, pp. 23–38.
56. D.M. Ebenstein and L.A. Pruitt: *Nano Today*, 2006, vol. 1, pp. 26–33.
57. L.L. Wu, L. Liu, M.S. Qi, J.H. Liu, R.J. Zhang (2012) *Advanced Materials Research*, vol. 562–564, Trans Tech Publications, Zurich, pp. 196–99.
58. P. Kucita, S.C. Wang, W.S. Li, R.B. Cook, and M.J. Starink: *J. Phys. Conf. Ser.*, 2015, vol. 644, art. no. 12010.
59. K.S. Lee and K. Yong-Nam: *Trans. Nonferrous Met. Soc. China*, 2013, vol. 23, pp. 341–46.
60. J. Chen, Y.N. Shi, and K. Lu: *J. Mater. Res.*, 2005, vol. 20, pp. 2955–59.
61. R.R. Chromik, R.P. Vinci, S.L. Allen, and M.R. Notis: *J. Mater. Res.*, 2003, vol. 18, pp. 2251–61.
62. J.Y. Zhang, J.T. Zhao, X.G. Li, Y.Q. Wang, K. Wu, G. Liu, and J. Sun: *Acta Mater.*, 2018, vol. 143, pp. 55–66.
63. F. Misjak, P.B. Barna, A.L. Toth, T. Ujvari, I. Bertoti, and G. Radnoezi: *Thin Solid Films*, 2008, vol. 516, pp. 3931–34.
64. B.J. Briscoe, L. Fiori, and E. Pelillo: *J. Phys. D: Appl. Phys.*, 1998, vol. 31, p. 2395.
65. M.M. Shokrieh, M.R. Hosseinkhani, M.R. Naimi-Jamal, and H. Tourani: *Polym. Test.*, 2013, vol. 32, pp. 45–51.
66. D. Beegan, S. Chowdhury, and M.T. Laugier: *Surf. Coat. Technol.*, 2005, vol. 192, pp. 57–63.
67. S.-R. Jian, C.-H. Tasi, S.-Y. Huang, and C.-W. Luo: *J. Alloys Compd.*, 2015, vol. 622, pp. 601–05.
68. B. Lauterbach and D. Gross: *Mech. Mater.*, 1998, vol. 29, pp. 81–92.
69. E. van der Heide, E.D. Stam, H. Giraud, G. Lovato, N. Akdut, F. Clarysse, P. Caenen, and I. Heikillä: *Wear*, 2006, vol. 261, pp. 68–73.

**Publisher's Note** Springer Nature remains neutral with regard to jurisdictional claims in published maps and institutional affiliations.